Global ocean carbon uptake enhanced by rainfall

Laetitia Parc, Hugo Bellenger, Laurent Bopp, Xavier Perrot, David T. Ho

nature geoscience

Article

https://doi.org/10.1038/s41561-024-01517-y

Global ocean carbon uptake enhanced by rainfall

Received: 11 January 2024

Accepted: 23 July 2024

Published online: 29 August 2024

Check for updates

Laetitia Parc [1] ✉, Hugo Bellenger [1] ✉, Laurent Bopp [1], Xavier Perrot [1] & David T. Ho [2,3]

Rain alters local sea surface physical and biogeochemical properties but its spatiotemporal variability has led to its overlook in global ocean carbon uptake studies. Different physical and chemical processes in the gaseous and liquid phases control the transfer of carbon dioxide (CO_2) between the atmosphere and ocean. Rain impacts the interfacial flux by (1) increasing turbulence in the ocean and (2) modulating the air–sea CO_2 concentration gradient. Concurrently, raindrops inject CO_2 absorbed during their fall into the ocean through wet deposition. Here this study presents a comprehensive estimate of these effects on the global ocean carbon uptake over 2008–2018 based on observational products (satellite and in situ) and reanalysis. Using various representations of the ocean surface response to rainfall and different rain products, we show that rain increases the ocean carbon sink by +0.14–0.19 PgC yr^{-1} over 2008–2018, representing an increase of 5–7% of the ocean carbon uptake (2.66 PgC yr^{-1}). Rain-induced interfacial flux and wet deposition have comparable orders of magnitude. The former mainly increases the CO_2 sink in the tropics because strong rain rates and weak winds induce noticeable salinity and CO_2 dilution. The latter is important in the tropics, storm track regions and the Southern Ocean.

Carbon dioxide (CO_2) emissions from human activities—principally through fossil fuel burning, cement manufacturing and land-use changes—have caused an increase in global temperature and subsequent changes in the climate system. A fraction of the CO_2 emissions is absorbed by the ocean, mitigating the increase in atmospheric CO_2 and alleviating some of the impacts of climate change. According to the 2022 assessment of the Global Carbon Budget (GCB)[1], the ocean uptake has remained relatively constant from 1960 to 2022, accounting for an average of 25% of total anthropogenic emissions. This estimate consolidates results from two different methodologies. The first approach is based on an ensemble of global ocean biogeochemical models forced by atmospheric reanalyses, while the second approach involves an ensemble of data-based products derived from the Surface Ocean CO_2 Atlas[2]. However, the GCB has also underscored substantial uncertainties between estimates from models and data-based products. For instance, recent research[3,4] suggests that all estimates of the ocean carbon sink may be underestimated by about 5–15% due to the oversight of temperature corrections in the ocean's diffusive skin. Furthermore, other processes, including bubbles and sea sprays generated by wave breaking, exert considerable influence on gas exchanges at the air–sea interface, especially on gas transfer velocities at high wind speeds[5–11]. This emphasizes the critical need for further exploring the role of small-scale processes on CO_2 exchanges at the ocean interface.

Rainfall over the ocean complicates the conventional way of estimating air–sea CO_2 fluxes, typically involving the calculation of a gas transfer velocity as a function of wind speed and determining the difference in CO_2 partial pressure (pCO_2) across the sea–air interface using either global ocean biogeochemical models or in situ measurements usually taken few metres below the ocean surface. First, several laboratory studies have shown that rain can enhance gas exchange in both fresh and salt water environments[12,13]. The penetration of raindrops in the first few centimetres below the ocean surface induces near-surface

[1]LMD/IPSL, ENS, Université PSL, École Polytechnique, Institut Polytechnique de Paris, Sorbonne Université, CNRS, Paris, France. [2]Department of Oceanography, University of Hawai'i at Mānoa, Honolulu, HI, USA. [3][C]Worthy, Boulder, CO, USA. ✉e-mail: parc.laetitia@gmail.com; hugo.bellenger@lmd.ipsl.fr

https://doi.org/10.1038/s41561-024-01517-y

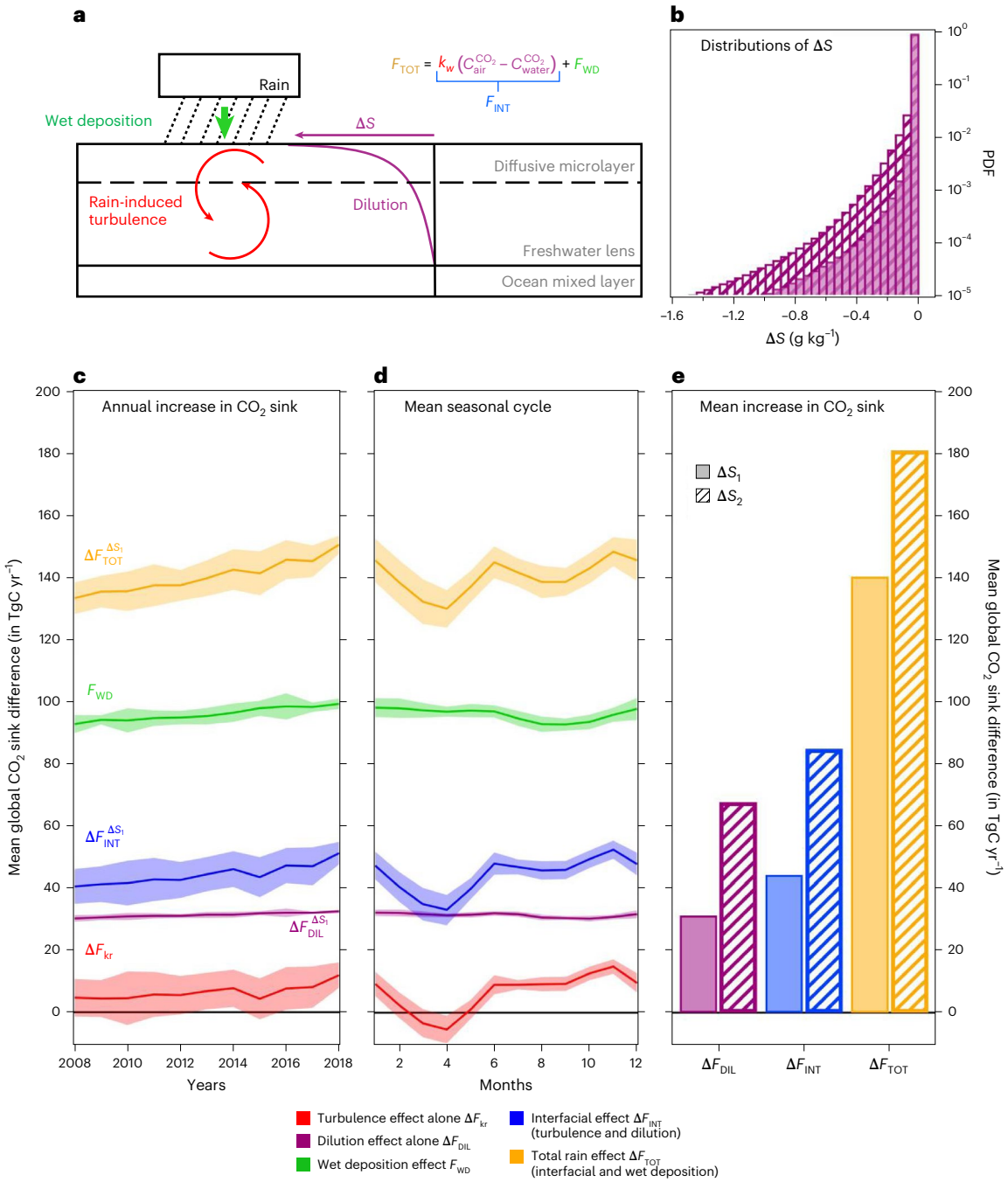

Fig. 1 | Rain impacts on CO_2 flux and sensitivity to dilution model. **a**, A schematic illustration of the different effects of rain on the CO_2 fluxes at the air–sea interface. **b**, The probability distribution function (PDF) of the rain-induced salinity dilution based on the prognostic scheme[30] ΔS_1 (shaded) and the satellite-derived parameterization[31] ΔS_2 (striped). **c**, A time series of the annual mean global ocean CO_2 sink differences (TgC yr^{-1}) due to the rain-induced turbulence effect ΔF_{kr} (red), the wet deposition effect F_{WD} (green), the rain-induced dilution effect $\Delta F_{DIL}^{\Delta S_1}$ (purple), the interfacial rain effect $\Delta F_{INT}^{\Delta S_1}$ (blue) and the total rain effect $\Delta F_{TOT}^{\Delta S_1}$ (orange) (shadings are the intra-annual s.d. of the corresponding differences). **d**, A time series of the monthly mean seasonal cycle of global CO_2 sink differences (in TgC yr^{-1}, colours are as in **c** and shading represents the interannual s.d. for each month). **e**, The mean 2008–2018 differences in global carbon sink due to ΔF_{DIL}, ΔF_{INT} and ΔF_{TOT} for both dilution parameterizations (in TgC yr^{-1}, colours are as in **c** and patterns are as in **b**).

turbulence[14,15], potentially increasing the gas transfer velocity. Furthermore, rain events alter the chemical and physical properties of the ocean surface layer[16–21] and can even result in the formation of freshwater lenses that can persist for hours after rainfall ceases[22–24]. By adding fresher and usually colder water just beneath the ocean surface, rain systematically diminishes sea surface pCO_2 through the dilution of dissolved inorganic carbon (DIC) and total alkalinity (TAlk)[21,25]. These changes in pCO_2, mainly occurring within the first metre of the ocean, are not detected in measurements typically acquired at 5–7 m depth using the seawater intakes of research vessels. This discrepancy could lead to substantial biases in regions with substantial rainfall. Lastly, raindrops directly inject CO_2 absorbed during their fall into the ocean surface layer[26]. Indeed, the pCO_2 in the raindrops is thought to be at equilibrium with the pCO_2 in the atmosphere when reaching the ocean surface[27], resulting in direct (or wet) deposition that adds to the conventional air–sea CO_2 flux.

So far, only two studies[26,28] have provided global estimates of the effects of rain on global CO_2 uptake. However, these studies only accounted for rain-induced turbulence and wet deposition, neglecting the substantial impact of rain-induced dilution. Conversely, while an evaluation of all these rain-induced effects on the carbon uptake has been conducted, it was limited to the year 2002 at a specific equatorial Pacific mooring location[29], highlighting the relative importance of rain-induced dilution.

Thus, this study aims to quantify the diverse effects of rain on the global ocean carbon uptake over the period 2008–2018. We compute the CO_2 flux using observational products (satellite and in situ) and reanalysis taking into account the thermohaline stratification within the first metres below the air–sea interface (Methods and Extended Data Figs. 1 and 2). These effects, schematized in Fig. 1a, are (1) the rain-induced turbulence, (2) the dilution and cooling of the ocean surface layer that impacts the CO_2 fugacity differences across the air–sea interface and (3) the direct wet deposition of CO_2 dissolved in raindrops (F_{WD}). We diagnose the change in CO_2 flux due to the rain-induced turbulence alone as ΔF_{kr} and the change due to the rain dilution alone as ΔF_{DIL}. The combination of both effects is called the interfacial rain effect and is noted ΔF_{INT}. The magnitude of the dilution effect depends strongly on how surface salinity responds to rain (Methods, Fig. 1b and Extended Data Fig. 3). Therefore, two parameterizations of the dilution in the ocean near surface are used: a prognostic model[30], ΔS_1, and a satellite-derived empirical parameterization[31], ΔS_2. Finally, we evaluate the sensitivity of these estimates to rain characteristics using two products characterized by different rain rate distributions.

Rain impact on the global ocean carbon sink

When considering all rain effects on air–sea CO_2 flux (ΔF_{TOT})—namely rain-induced turbulence, ocean surface dilution and wet deposition—rain leads to a total average increase in the global (90° N–90° S) ocean carbon uptake F_{ref} of 140–180 TgC yr^{-1} (teragrams of carbon per year), thus representing 5.3–6.9% of F_{ref} (Table 1 and Fig. 1e). This range is attributed to the uncertainty associated to the surface dilution effect evaluated through two distinct parameterizations (Fig. 1b,e). It shows an increasing trend of ~16–19 TgC yr^{-1} per decade (Fig. 1c and Extended Data Fig. 4a) as well as seasonal amplitude of around 19 TgC yr^{-1} (Fig. 1d and Extended Data Fig. 4b). This total rain effect is further decomposed as the sum of two components: the interfacial rain effect ΔF_{INT} and wet deposition F_{WD}.

Wet deposition emerges as the largest effect on the global ocean CO_2 sink, with an average increase of 97.0 TgC yr^{-1} (3.6% of F_{ref}; Table 1). This effect scales linearly with global rain rate. There is also a decadal positive trend of 6.0 TgC yr^{-1} per decade (Fig. 1c) and a weak seasonal variation (Fig. 1d). Finally, the spatial variability of the wet deposition effect F_{WD} reflects the mean spatial distribution of rainfall (Fig. 2c), with local maximum reaching +1 gC m^{-2} yr^{-1} in the Inter-tropical Convergence Zone (ITCZ).

The total interfacial rain effect ΔF_{INT}, combining the effects of rain-induced turbulence and dilution, is substantially stronger than the impact of each contributing factor (discussed below). This remains consistent regardless of the representation of rain-induced freshening chosen for the analysis. Using the physically based parameterization[30] to compute $\Delta F_{INT}^{\Delta S_1}$, the increase of the global CO_2 sink is estimated to be 44.8 TgC yr^{-1} (1.7% of F_{ref}; Table 1 and Fig. 1e). Using the satellite-derived parameterization[31], $\Delta F_{INT}^{\Delta S_2}$ leads to an increase of 85.9 TgC yr^{-1} (3.2% of F_{ref}; Table 1 and Fig. 1e). Our analysis reveals interannual trends of ~10 TgC yr^{-1} per decade for $\Delta F_{INT}^{\Delta S_1}$ (Fig. 1c) and ~13 TgC yr^{-1} per decade for $\Delta F_{INT}^{\Delta S_2}$ (Extended Data Fig. 4a). Seasonal fluctuations (Fig. 1d and Extended Data Fig. 4b) of ~20 TgC yr^{-1} seem attributed solely to the seasonal variations in the rain-induced turbulence effect. Both interfacial rain effects, $\Delta F_{INT}^{\Delta S_1}$ and $\Delta F_{INT}^{\Delta S_2}$, are found to have a maximum impact on the global carbon uptake in the ITCZ over the warm pool (Fig. 2a,b). In this region, the flux increase reaches +0.5 gC m^{-2} yr^{-1} for $\Delta F_{INT}^{\Delta S_1}$ and +1 gC m^{-2} yr^{-1} for $\Delta F_{INT}^{\Delta S_2}$ on average from 2008 to 2018. The latter estimate derived from the satellite-based parameterization[31] also indicates a noticeable enhancement of CO_2 absorption at higher latitudes, such as in the storm track regions of the Gulf Stream and Kuroshio and in the Southern Ocean (Fig. 2b).

The individual effect of rain-induced turbulence alone, ΔF_{kr}, causes an average increase of the global ocean carbon sink of 6.6 TgC yr^{-1} (0.25% of F_{ref}; Table 1). Its annual contribution to the ocean CO_2 fluxes appears relatively modest (Fig. 1c), stemming from compensating seasonal variations with increased CO_2 outgassing in March and April and increased sink during the rest of the year (Fig. 1d). The effect of rain-induced turbulence peaks in the tropics, in particular in the equatorial regions of the Pacific and Atlantic oceans (Fig. 2d). In these regions of relatively weak winds (below 5 m s^{-1}), rain tends to increase the total transfer velocity $k(600)_t$ by up to 10–15% (Fig. 2d).

Rain-induced dilution affects CO_2 concentrations, defined as the product of CO_2 solubility and fugacity, across the air–sea interface, but its amplitude is uncertain (Methods). Using the satellite-derived empirical relationship[31] leads to a CO_2 uptake increase of 68.5 TgC yr^{-1} (2.6% of F_{ref}), whereas the prognostic scheme[30] leads to a more moderate increase of 31.7 TgC yr^{-1} representing 1.2% of F_{ref} (Table 1 and Fig. 1e). Notably, this rain-induced dilution effect exhibits no discernible interannual or seasonal variations, regardless of the chosen parameterization (Fig. 1c,d and Extended Data Fig. 4). Rain induces dilution and cooling in the diffusive microlayer, consequently altering both the temperature T_{int} and salinity S_{int} at the interface. Given that the concentration at the interface C_{int} decreases with both increasing

Table 1 | CO_2 fluxes calculation results for both domains of study (90° N–90° S and 60° N–60° S)

Spatial domain	90° N–90° S	60° N–60° S	60° N–60° S
Reference ocean carbon sink	+2.66 (±0.21)	+2.49 (±0.20)	+2.49 (±0.20)
Rain products	**ERA5**	**ERA5**	**IMERG**
Rain-induced turbulence effect ΔF_{kr}	+7.10^{-3} (0.25%, ±2.10^{-3})	+6.10^{-3} (0.25%, ±2.10^{-3})	+0.01 (0.4%, ±2.10^{-3})
Rain-induced dilution effect $\Delta F_{DIL}^{\Delta S_1}$	+0.03 (1.2%, ±7.10^{-4})	+0.03 (1.2%, ±6.10^{-4})	+0.025 (1.0%, ±6.10^{-4})
Rain-induced dilution effect $\Delta F_{DIL}^{\Delta S_2}$	+0.07 (2.6%, ±1.10^{-3})	+0.065 (2.6%, ±1.10^{-3})	+0.06 (2.5%, ±1.10^{-3})
Interfacial rain effect $\Delta F_{INT}^{\Delta S_1}$	+0.04 (1.7%, ±3.10^{-3})	+0.04 (1.7%, ±3.10^{-3})	+0.05 (2.0%, ±2.10^{-3})
Interfacial rain effect $\Delta F_{INT}^{\Delta S_2}$	+0.09 (3.2%, ±4.10^{-3})	+0.08 (3.3%, ±4.10^{-3})	+0.10 (3.9%, ±3.10^{-3})
Wet deposition effect F_{WD}	+0.10 (3.6%, ±2.10^{-3})	+0.09 (3.7%, ±2.10^{-3})	+0.09 (3.8%, ±2.10^{-3})
Total rain effect $\Delta F_{TOT}^{\Delta S_1}$	+0.14 (5.3%, ±5.10^{-3})	+0.13 (5.4%, ±5.10^{-3})	+0.14 (5.7%, ±4.10^{-3})
Total rain effect $\Delta F_{TOT}^{\Delta S_2}$	+0.18 (6.9%, ±6.10^{-3})	+0.17 (7.0%, ±6.10^{-3})	+0.19 (7.7%, ±5.10^{-3})

This table contains the mean values of the 2008–2018 annual global sink (in petagrams of carbon per year, PgC yr^{-1}) for the reference case F_{ref}, with the corresponding year-to-year s.d. provided in parentheses. Additionally, the mean values of 2008–2018 annual global carbon sink differences (PgC yr^{-1}) due to the different rain effects are also provided for both dilution parameterizations and global rain products, the corresponding relative difference to the reference carbon sink F_{ref} and year-to-year s.d. given in parentheses. All fluxes are calculated using ERA5 reanalysis[36], a global sea surface salinity dataset from multivariate observations[37,38], the National Oceanic and Atmospheric Administration (NOAA) Greenhouse Gas Marine Boundary Layer Reference for the atmospheric CO_2 data[39] and the OceanSODA-ETHZ climatology dataset[40] for the DIC and TAlk fields. The different rain effects are calculated using either ERA5 reanalysis rain data[36] or Integrated Multi-satellitE Retrievals for GPM (IMERG) satellite-based rain estimates[41].

https://doi.org/10.1038/s41561-024-01517-y

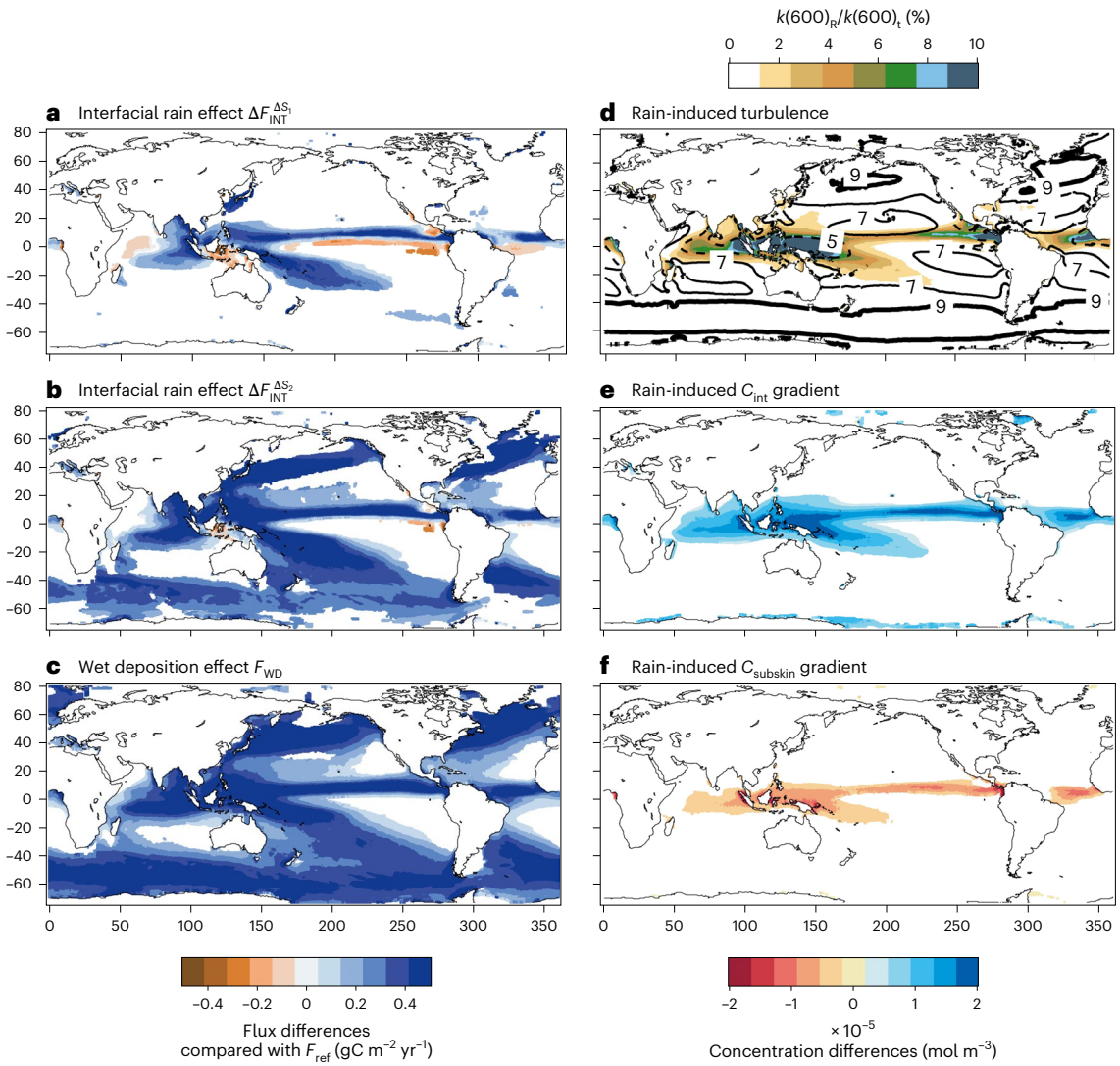

Fig. 2 | Spatial distribution of distinct rain effects. a–c, Mean maps of the interfacial rain effects using the physically based parameterization[30] $\Delta F_{INT}^{\Delta S_1}$ (gC m^{-2} yr^{-1}) (**a**), using the satellite-derived parameterization[31] $\Delta F_{INT}^{\Delta S_2}$ (gC m^{-2} yr^{-1}) (**b**) and the wet deposition effect F_{WD} (gC m^{-2} yr^{-1}) (**c**) over the period 2008–2018. **d**, Mean map of the ratio of the rain contribution to the transfer velocity $k(600)_R$ with the total transfer velocity $k(600)_t$ (%). The black contours represent the annual mean wind speed (m s^{-1}) from ERA5 for u_{10} = 5 m s^{-1} (dashed line), u_{10} = 7 m s^{-1} (thin line) and u_{10} = 9 m s^{-1} (thick line). **e**,**f**, Maps of mean rain-induced CO_2 concentration differences (mol m^{-3}) at the interface (**e**) and the bottom of the diffusive microlayer (**f**) using the prognostic model[30] ΔS_1 over the 11 year study. Only the air–sea CO_2 flux and concentration differences *t*hat are statistically significant at the 99% level estimated by the Student's *t*-test are plotted.

temperature and salinity, dilution leads to its increase and, thus, the increase of CO_2 sink. This is the case in the tropical regions, the ITCZ and the South Pacific Convergence Zone (Fig. 2e). These changes in C_{int} primarily result from rain-induced decreases in S_{int} (Extended Data Fig. 5a–c), leading to an increase of the CO_2 sink in the tropics (Fig. 2a). Furthermore, rain impacts the temperature, salinity, DIC and TAlk below the ocean skin, which in turn alter the water-side CO_2 concentration in the subskin layer, $C_{subskin}$. Rain causes a decrease in $C_{subskin}$ and thus an increase in CO_2 sink, which is dominated by the decrease in salinity, DIC and TAlk at the bottom of the diffusive microlayer[4,32] (Extended Data Fig. 5d–f). This effect is also spatially limited to the tropical regions (Fig. 2f).

Sensitivity to rain rates

Wet deposition, as parameterized[26], scales linearly with the rain rate and, therefore, only depends on the total amount of rain. The rain impact on the interfacial CO_2 flux is, however, nonlinear. Specifically, the subskin dilution relationship with rain rate demonstrates a nonlinear dependency[4,31,33]. To assess the rain-induced nonlinear increase in the global ocean CO_2 sink, two global rain datasets, ERA5 and IMERG, with comparable overall rain amounts but distinct rain rate distributions, were considered. Indeed, over the 2008–2018 period and 60° N–60° S, their respective total quantity of rain is: 1.24 × 10^3 kg m^{-2} yr^{-1} for ERA5 and 1.27 × 10^3 kg m^{-2} yr^{-1} for IMERG, but with noticeably different rain rate distributions (Fig. 3a,b). Large rain rates of more than 10 mm h^{-1} contribute considerably to the total rainfall (around 15%) for IMERG, but to less than 2% for ERA5 (Fig. 3b).

The higher rain rates from IMERG lead to an increase in the interfacial CO_2 flux (Table 1 and Fig. 3c) for both parameterizations representing ocean surface dilution. Thus, for 2008–2018 and 60° N–60° S, $\Delta F_{INT}^{\Delta S_2}$ increases from an average of 82.5 TgC yr^{-1} to 96.9 TgC yr^{-1} with IMERG (+17.5%), while $\Delta F_{INT}^{\Delta S_1}$ increases from 42.8 TgC yr^{-1} to 48.7 TgC yr^{-1} (+14%). Wet deposition remains constant (+2% for F_{WD} using IMERG compared with ERA5) as both datasets have comparable total rain amounts. Therefore, employing a dataset with stronger and more realistic rain rates results in an increase in the total rain effect on the CO_2 sink by 0.14–0.19 PgC yr^{-1}, representing 5.7–7.7% of the 60° N–60° S ocean sink. Finally, the trend showing a temporal increase

https://doi.org/10.1038/s41561-024-01517-y

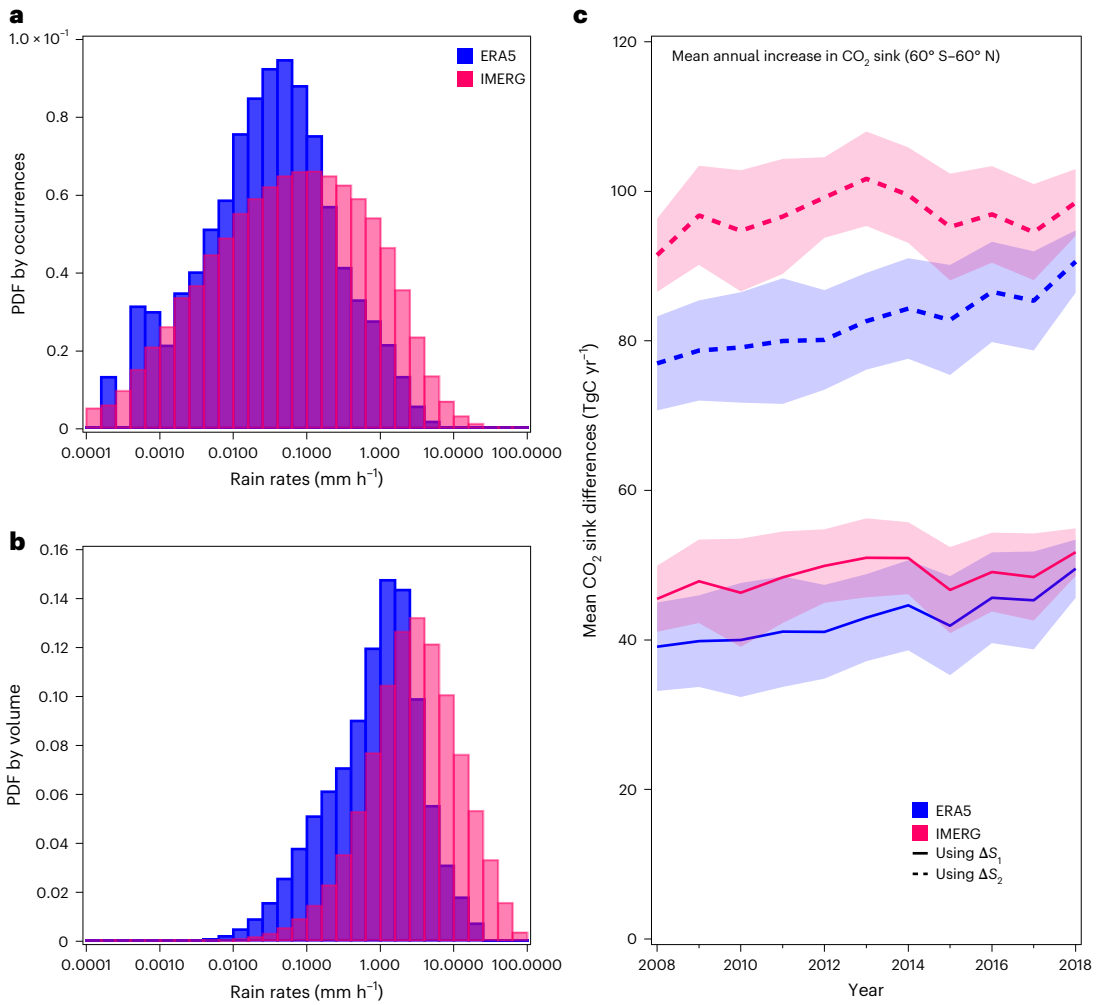

Fig. 3 | Sensitivity to rain rate distributions. a,**b**, The probability distribution function (PDF) by occurrences (**a**) and by volume (**b**) of non-null rainfall datasets from ERA5 (blue) and IMERG (pink) over the domain 60° S–60° N from 2008 to 2018. **c**, Time series of the annual mean increase in the ocean CO_2 sink (TgC yr^{-1}) due to the interfacial rain effects $\Delta F_{INT}^{\Delta S_1}$ (solid lines) and $\Delta F_{INT}^{\Delta S_2}$ (dashed lines) calculated using ERA5 rain dataset[36] (blue lines) and IMERG rain dataset[41] (pink lines) over the period 2008–2018 and the spatial domain 60° S–60° N (shadings are the intra-annual standard deviation of the corresponding differences).

in rain-induced interfacial flux as seen with ERA5 (Figs. 1c and 3c) is not evident when using IMERG (Fig. 3c). Unlike ERA5, IMERG does not show any clear trend in the global rain amount over 2008–2018.

The upper limit of our diagnostics is given by $\Delta F_{TOT}^{\Delta S_2}$ using IMERG, which is +0.19 PgC yr^{-1} on 60° S–60° N. It represents 7.1% of the global (90° S–90° N) reference flux F_{ref} of 2.66 PgC yr^{-1}. Using ERA5, the total rain effect poleward of 60° represents only 5% of the total effect over the whole globe (90° S–90° N). As ERA5 cannot be validated against IMERG poleward of 60°, the most conservative hypothesis is to consider that this 7.1% increase represents an upper limit for the global (90° S–90° N) effect of rain on the CO_2 sink.

Relevance of rain effects for future carbon budgets

This study provides the first comprehensive estimate of the rain impact on the global ocean CO_2 sink. For the period 2008–2018, rain induces an increase in the global ocean carbon sink of 5–7%, representing an additional absorption of 0.14–0.19 PgC yr^{-1} on average, depending on the dilution parameterization and on the quality of the dataset's rain rate distribution. The main regions affected by rain are, as expected from previous studies, the tropical regions, especially the ITCZ and South Pacific Convergence Zone, characterized by strong rainfall and weak winds. However, rain also impacts carbon uptake in higher latitude regions characterized by stronger winds, such as the storm track regions and the Southern Ocean.

Rainfall over the ocean acts like a river with no defined length that directly flows to the ocean. Much like rivers, rain inputs CO_2 into the ocean through two primary mechanisms: (1) rain injects a certain amount of CO_2 that it has collected during its fall (the wet deposition) and (2) because this amount of CO_2 corresponds to weak concentrations, rain also dilutes the near-surface ocean waters, increasing the air–sea transfer of CO_2 (the interfacial flux).

Wet deposition appears to have the most prominent impact of rain on the global ocean CO_2 sink. However, as in situ measurements of the concentration of CO_2 in raindrops are particularly challenging, its parameterization has predominantly arisen from theoretical calculations[27]. Our estimate of 97.0 TgC yr^{-1} for the global wet deposition is consistent with the 90.0 TgC yr^{-1} found in a previous single-year study[26] for 2001 and 40% larger than the 61.4 TgC yr^{-1} found in the most recent global study[28] for the 1999–2006 period.

Finally, previous global estimates[26,28] have only considered the enhancement of near-surface turbulence by rain ΔF_{kr} as the interfacial rain effect ΔF_{INT}, without considering the associated effect of dilution. This study shows that this leads to a noticeable underestimation of ΔF_{INT}. Indeed, while ΔF_{kr} alone increases the global carbon sink by a few TgC yr^{-1} (refs. 26,28), taking into account dilution amplifies these

figures by factors of 10–20. As the satellite-derived parameterization of dilution[31] has been developed based on a large sample of IMERG rain events and collocated salinity anomalies from Soil Moisture and Ocean Salinity (SMOS) and Soil Moisture Active and Passive (SMAP) satellite measurements, its diagnostic of dilution and, thus, rain effect appear more statistically robust than estimates based on the physically based parameterization. However, in situ measurements in a mid-latitude region have shown that linear relationships between salinity anomalies, rain and wind speeds could lead to overestimation of dilution[22], especially in the case of advection, limiting the accuracy of the upper bound of this diagnostic.

Hence, it is imperative to incorporate rain effects into ocean and climate models, particularly in the context of global carbon budgets. As shown in a recent study[4], the magnitude of the ocean skin effect on the global ocean carbon uptake is dampened in a coupled model framework, as the resulting accumulation of CO_2 in the surface ocean reduces the flux at the atmosphere–ocean interface. Similarly, the impact of rain is anticipated to diminish when evaluated in the same framework. However, this decline should not impede wet deposition, which relies solely on the mole fraction of atmospheric CO_2. Furthermore, as climate projections indicate a potential intensification of rainfall rates in a warming climate[34,35], this could lead to an increase in the rain impact on the global ocean CO_2 flux. Nevertheless, an accurate quantification of rain effects using climate models faces challenges due to their coarse horizontal resolution, limiting their capacity to replicate realistic rain rate distributions.

Online content

Any methods, additional references, Nature Portfolio reporting summaries, source data, extended data, supplementary information, acknowledgements, peer review information; details of author contributions and competing interests; and statements of data and code availability are available at https://doi.org/10.1038/s41561-024-01517-y.

References

1. Friedlingstein, P. et al. Global carbon budget 2023. *Earth Syst. Sci. Data* **15**, 5301–5369 (2023).
2. Bakker, D. C. E. et al. A multi-decade record of high-quality fCO_2 data in version 3 of the Surface Ocean CO_2 Atlas (SOCAT). *Earth Syst. Sci. Data* **8**, 383–413 (2016).
3. Watson, A. J. et al. Revised estimates of ocean-atmosphere CO_2 flux are consistent with ocean carbon inventory. *Nat. Commun.* **11**, 4422 (2020).
4. Bellenger, H. et al. Sensitivity of the global ocean carbon sink to the ocean skin in a climate model. *J. Geophys. Res. Oceans* **128**, e2022JC019479 (2023).
5. Bell, T. G. et al. Estimation of bubble-mediated air–sea gas exchange from concurrent DMS and CO_2 transfer velocities at intermediate–high wind speeds. *Atmos. Chem. Phys.* **17**, 9019–9033 (2017).
6. Blomquist, B. W. et al. Wind speed and sea state dependencies of air–sea gas transfer: results from the high wind speed gas exchange study (HiWinGS). *J. Geophys. Res. Oceans* **122**, 8034–8062 (2017).
7. Gutiérrez-Loza, L., Nilsson, E., Wallin, M. B., Sahlée, E. & Rutgersson, A. On physical mechanisms enhancing air–sea CO_2 exchange. *Biogeosciences* **19**, 5645–5665 (2022).
8. Fairall, C. W., Hare, J. E., Edson, J. B. & McGillis, W. Parameterization and micrometeorological measurement of air–sea gas transfer. *Bound. Layer Meteorol.* **96**, 63–106 (2000).
9. Hare, J. E. et al. Evaluation of the National Oceanic and Atmospheric Administration/Coupled-Ocean Atmospheric Response Experiment (NOAA/COARE) air–sea gas transfer parameterization using GasEx data. *J. Geophys. Res. Oceans* **109**, 2003JC001831 (2004).
10. Andreas, E., Vlahos, P. & Monahan, E. Spray-mediated air–sea gas exchange: the governing time scales. *J. Mar. Sci. Eng.* **5**, 60 (2017).
11. Staniec, A., Vlahos, P. & Monahan, E. C. The role of sea spray in atmosphere–ocean gas exchange. *Nat. Geosci.* **14**, 593–598 (2021).
12. Ho, D. T., Bliven, L. F., Wanninkhof, R. & Schlosser, P. The effect of rain on air–water gas exchange. *Tellus B* **49**, 149–158 (1997).
13. Ho, D. T. et al. Influence of rain on air-sea gas exchange: lessons from a model ocean. *J. Geophys. Res. Oceans* **109**, 2003JC001806 (2004).
14. Ho, D. T., Asher, W. E., Bliven, L. F., Schlosser, P. & Gordan, E. L. On mechanisms of rain-induced air–water gas exchange. *J. Geophys. Res. Oceans* **105**, 24045–24057 (2000).
15. Takagaki, N. & Komori, S. Effects of rainfall on mass transfer across the air–water interface. *J. Geophys. Res. Oceans* **112**, 2006JC003752 (2007).
16. Henocq, C. et al. Vertical variability of near-surface salinity in the tropics: consequences for l-band radiometer calibration and validation. *J. Atmos. Ocean. Technol.* **27**, 192–209 (2010).
17. Reverdin, G., Morisset, S., Boutin, J. & Martin, N. Rain-induced variability of near sea-surface *T* and *S* from drifter data. *J. Geophys. Res. Oceans* **117**, C02032 (2012).
18. Asher, W. E., Jessup, A. T., Branch, R. & Clark, D. Observations of rain-induced near-surface salinity anomalies. *J. Geophys. Res. Oceans* **119**, 5483–5500 (2014).
19. Boutin, J. et al. Sea surface salinity under rain cells: SMOS satellite and in situ drifters observations. *J. Geophys. Res. Oceans* **119**, 5533–5545 (2014).
20. Volkov, D., Dong, S., Foltz, G., Goni, G. & Lumpkin, R. Observations of near-surface salinity and temperature structure with dual-sensor Lagrangian drifters during SPURS-2. *Oceanography* **32**, 66–75 (2019).
21. Ho, D. T. & Schanze, J. J. Precipitation-induced reduction in surface ocean pCO_2: observations from the Eastern Tropical Pacific Ocean. *Geophys. Res. Lett.* **47**, e2020GL088252 (2020).
22. Ten Doeschate, A. et al. Upper ocean response to rain observed from a vertical profiler. *J. Geophys. Res. Oceans* **124**, 3664–3681 (2019).
23. Reverdin, G. et al. Intense and small freshwater pools from rainfall investigated during Spurs-2 on 9 November 2017 in the Eastern Tropical Pacific. *J. Geophys. Res. Oceans* **125**, e2019JC015558 (2020).
24. Moulin, A. J., Moum, J. N., Shroyer, E. L. & Hoecker-Martínez, M. Freshwater lens fronts propagating as buoyant gravity currents in the equatorial Indian Ocean. *J. Geophys. Res. Oceans* **126**, e2021JC017186 (2021).
25. Sarmiento, J. L. & Gruber, N. *Ocean Biogeochemical Dynamics* (Princeton Univ. Press, 2006).
26. Komori, S., Takagaki, N., Saiki, R., Suzuki, N. & Tanno, K. in *Transport at the Air-Sea Interface* (eds Garbe, C. S., Handler, R. A. & Jähne, B.) 169–179 (Springer, 2007).
27. Sugioka, K.-I. & Komori, S. Drag and lift forces acting on a spherical water droplet in homogeneous linear shear air flow. *J. Fluid Mech.* **570**, 155–175 (2007).
28. Ashton, I. G., Shutler, J. D., Land, P. E., Woolf, D. K. & Quartly, G. D. A sensitivity analysis of the impact of rain on regional and global sea–air fluxes of CO_2. *PLoS ONE* **11**, e0161105 (2016).
29. Turk, D. et al. Rain impacts on CO_2 exchange in the western equatorial Pacific Ocean. *Geophys. Res. Lett.* **37**, L23610 (2010).
30. Bellenger, H. et al. Extension of the prognostic model of sea surface temperature to rain-induced cool and fresh lenses. *J. Geophys. Res. Oceans* **122**, 484–507 (2017).
31. Supply, A., Boutin, J., Reverdin, G., Vergely, J.-L. & Bellenger, H. in *Satellite Precipitation Measurement* (eds Levizzani, V. et al.) vol. 69 1155–1176 (Springer, 2020).

32. Woolf, D. K., Land, P. E., Shutler, J. D., Goddijn-Murphy, L. M. & Donlon, C. J. On the calculation of air-sea fluxes of CO_2 in the presence of temperature and salinity gradients. *J. Geophys. Res. Oceans* **121**, 1229–1248 (2016).
33. Drushka, K., Asher, W. E., Ward, B. & Walesby, K. Understanding the formation and evolution of rain-formed fresh lenses at the ocean surface. *J. Geophys. Res. Oceans* **121**, 2673–2689 (2016).
34. Pendergrass, A. G., Knutti, R., Lehner, F., Deser, C. & Sanderson, B. M. Precipitation variability increases in a warmer climate. *Sci. Rep.* **7**, 17966 (2017).
35. Pendergrass, A. G. The global-mean precipitation response to CO_2-induced warming in CMIP6 models. *Geophys. Res. Lett.* **47**, e2020GL089964 (2020).
36. Hersbach, H. et al. The ERA5 global reanalysis. *Q. J. R. Meteorol. Soc.* **146**, 1999–2049 (2020).
37. Droghei, R., Buongiorno Nardelli, B. & Santoleri, R. Combining in situ and satellite observations to retrieve salinity and density at the ocean surface. *J. Atmos. Ocean. Technol.* **33**, 1211–1223 (2016).
38. Droghei, R., Buongiorno Nardelli, B. & Santoleri, R. A new global sea surface salinity and density dataset from multivariate observations (1993–2016). *Front. Mar. Sci.* **5**, 84 (2018).
39. Lan, X., Tans, P., Thoning, K. & NOAA Global Monitoring Laboratory. NOAA greenhouse gas marine boundary layer reference—CO_2. *NOAA GML* https://doi.org/10.15138/DVNP-F961 (2023).
40. Gregor, L. & Gruber, N. OceanSODA–ETHZ: a global gridded data set of the surface ocean carbonate system for seasonal to decadal studies of ocean acidification. *Earth Syst. Sci. Data* **13**, 777–808 (2021).
41. Huffman, G., Stocker, E. F., Bolvin, D. T., Nelkin, E. J. & Tan, J. GPM IMERG final precipitation l3 half hourly 0.1 degree × 0.1 degree V07. *NASA Goddard Earth Sciences Data and Information Services Center* https://doi.org/10.5067/GPM/IMERG/3B-HH/07 (2023).

Methods

The CO_2 air–sea flux calculation

The air–sea CO_2 flux is classically diagnosed as proportional to the air–sea CO_2 concentration difference that can be expressed as the product of the aqueous-phase solubility coefficients of CO_2 (K_0) and CO_2 fugacity (fCO_2) as follows (positive into the ocean)[25]:

$$F_{CO_2} = k(600)\left(\frac{S_c(T)}{600}\right)^{-\frac{1}{2}}\left(K_0^a(T,S)fCO_2^a(T,S) - K_0^w(T,S)fCO_2^w(T,S)\right) \quad (1)$$

Where $k(S_c)$ is the gas transfer velocity for a given Schmidt number S_c. The Schmidt number is the kinematic viscosity of water divided by the diffusion coefficient of a given gas, here CO_2, in water and is determined as a function of temperature and, to a lesser extent, salinity[42,43]. For CO_2 and in the case of freshwater, the Schmidt number is $S_c = 600$ at $T = 20\,°C$. Generally, the gas transfer velocity is parameterized as a function of wind speed only[42,44–47] and, following open ocean dual tracer experiments[47], it can be defined by:

$$k(600) = k_u(600) = 0.266u_{10}^2 \quad (2)$$

where $k_u(600)$ is the wind-induced gas transfer velocity. The CO_2 aqueous-phase solubility coefficients in the ocean (K_0^w) and at the interface (K_0^a) represent the amount of gaseous CO_2 that dissolves in a given volume of seawater as functions of temperature and salinity[48]. Additionally, fCO_2^w and fCO_2^a are the fugacity of CO_2 in the ocean and in the atmosphere respectively, which are defined as effective partial pressures taking into account the non-ideal behaviour of CO_2 gases. The atmospheric CO_2 fugacity, fCO_2^a, is a function of atmospheric mole fraction of CO_2, atmospheric surface pressure, partial pressure of water vapour and a fugacity coefficient, with the last two quantities being functions of temperature and salinity[48,49]. Finally, the CO_2 fugacity in the ocean fCO_2^w is dependent on the thermodynamic equilibrium of the carbonate system in seawater. It can be computed as a function of temperature, salinity, DIC, TAlk, silicate and phosphate using the MOCSY package[50]. The formulation from Waters and Millero[51] has been chosen to compute the dissociation constants of carbonic acid (K_1 and K_2) because it is valid over the widest range of T and S. The concentrations of total inorganic boron B_T are based on Uppström[52] following best practices[53].

Usually, in global models and observations-derived products[1], estimates of the ocean carbon sink are calculated from equation (1) considering temperature and salinity representative of the ocean mixed layer (5–10 m depth), called foundation temperature T_{fnd} and salinity S_{fnd}. This flux is noted F_{fnd} in this study. However, this approach does not allow for accounting of substantial gradients in temperature and salinity that can form in the first metres of the upper ocean. Several phenomena can cause these thermohaline changes, which include the solar-induced formation of diurnal warm layers in the first few metres[54–56], particularly present in the tropics[57,58], as well as the formation of thermal and haline diffusive microlayers of less than a millimetre thick directly below the ocean interface[56,59,60]. Therefore, the CO_2 flux should be evaluated from the concentration difference across the molecular boundary layer[61,62], leading to a substantial impact of this ocean skin on the global CO_2 sink[3,4,32,63,64].

In this study, the reference flux F_{ref} is calculated by taking into account the thermohaline stratification within the first metres below the ocean surface due to the ocean's 'cool skin' and the formation of diurnal warm layers. This reference flux is computed as:

$$F_{ref} = k(600)\left(\frac{S_c(T_{int})}{600}\right)^{-\frac{1}{2}}\left(K_{0int}^a fCO_{2int}^a - K_{0subskin}^w fCO_{2subskin}^w\right) \quad (3)$$

where subscript int denotes that the quantity is evaluated at the interface and subskin below the diffusive microlayer (Extended Data Fig. 1). Note that because molecular diffusivity of salt and heat are different, the depths of both diffusive microlayers, respectively δ_S and δ_T, are markedly distinct (Extended Data Fig. 1) with $\delta_T \sim 100\,\mu m$ and $\delta_S \sim 10\,\mu m$. CO_2 flux should be evaluated from temperature and salinity at the top and bottom of the haline microlayer[62]. However, the residence time of water parcels in this microlayer is usually shorter than the chemical equilibrium timescale[32,64]. Therefore, in what is called the 'rapid model', the temperature and salinity at the base of the thermal microlayer are used to compute $fCO_{2subskin}^w$. In the following, the subscript subskin refers to the base of the thermal diffusive microlayer.

To validate our estimates of the global ocean carbon uptake using the bulk flux parameterization F_{fnd} and of the impact of the ocean skin and formation of diurnal warm layers considered in our reference case F_{ref}, we compare them with estimates provided by the GCB[1] and the SeaFlux data product[65]. The global mean ocean CO_2 sink F_{fnd} from 2008 to 2018 is on average $2.36 \pm 0.21\,PgC\,yr^{-1}$. While this estimate is weaker than the estimate of the GCB ocean carbon sink including the diagnostics based on the different data products and models (Extended Data Fig. 2a, black line), their respective trends in the increase of the global ocean sink are comparable ($+0.07\,PgC\,yr^{-1}$ for F_{fnd} and $+0.05\,PgC\,yr^{-1}$ for GCB over 2008–2018). The flux estimate for the reference case, F_{ref}, is on average $2.66 \pm 0.21\,PgC\,yr^{-1}$ (Table 1) over the same period, the cool skin correction leading to an increase of the global carbon uptake by $+0.30\,PgC\,yr^{-1}$, which represents an increase of 13% of global carbon uptake over the period and is consistent with previous diagnostic studies[3,64]. Considering F_{fnd}, most regions of CO_2 outgassing are situated in the tropical and subtropical oceans with local minima around $-50\,gC\,m^{-2}\,yr^{-1}$ while the eastern Equatorial Pacific Ocean, subtropical and mid-latitude regions are mainly characterized by the absorption of CO_2 (Extended Data Fig. 2b). The mean flux can reach values around $+40\,gC\,m^{-2}\,yr^{-1}$ in the Northern Atlantic and Pacific oceans. When compared with the SeaFlux data product[65] (Extended Data Fig. 2d), the spatial distribution of F_{fnd} appears to be consistent in most regions. However, the equatorial Pacific Ocean CO_2 outgassing is overestimated by up to $-15\,gC\,m^{-2}\,yr^{-1}$, and the CO_2 sink in the high latitude regions by up to $+30\,gC\,m^{-2}\,yr^{-1}$.

The effects of rain on air–sea CO_2 fluxes

Rainfall has distinct effects on the physical and biogeochemical state of the surface ocean, as follows: (1) the penetration of raindrops in the first centimetres below the surface induces an enhancement of the turbulence at the interface[12–14,26,66–68] and (2) the associated input of fresh and usually cold water leads to salinity and temperature gradients. As raindrops are weakly concentrated in CO_2, they also dilute carbonate system variables in the first metres below the surface. Finally, (3) it directly injects moles of carbon into the ocean that raindrops absorb during their fall (wet deposition). Rainfall thus impacts fCO_{2int}^a and $fCO_{2subskin}^w$ through cooling and dilution of salinity, DIC and TAlk. While the evaluation of the salinity and TAlk dilution is done considering an input of freshwater ($S = 0$) with no alkalinity contribution, rain is weakly concentrated in DIC[21,26] with $DIC = DIC_r$. In addition to being responsible for the wet deposition, this rain DIC slightly limits the DIC dilution by rain. This effect is however negligible.

(1) Effect of rain on ocean near-surface turbulence. Following studies based on laboratory experiments[12,66], the enhancement of the transfer velocity by rain-induced turbulence is defined as an additional term. The total gas transfer velocity due to wind and rain ($k(600)_t$) is[66]:

$$k(600)_t = k(600)_u + k(600)_R = k(600)_u + \left(1 - \exp\left(-a\frac{KEF_R}{KEF_w}\right)\right)k(600)_{rain} \quad (4)$$

where $a = 0.3677$, $k(600)_{rain}$ the rain-induced transfer velocity, KEF_R and KEF_w are the kinetic energy fluxes imparted to the water by the rain and by the surface winds, respectively.

(2) Effect of rain on the near surface water composition. The variations in the temperature and salinity in the first metres below the ocean surface are calculated at 1 h interval at 0.25° resolution over the entire globe using a prognostic ocean skin model[30]. This latter determines the changes in temperature and salinity (1) across the diffusive microlayer (<1 mm thick) following Fairall et al.[56] for T and Schlüssel et al.[69] for S, and (2) below the skin and within the first metres by extending a sea surface skin temperature prognostic scheme[70] for diurnal warm layers so that it can represent the cooling and freshening of the near surface by rain (Extended Data Figs. 1 and 3a,b for the spatial distribution of rain-induced salinity anomalies in the ocean near surface). The input variables for the model are T_{fnd}, S_{fnd}, rain rate ((R), 10 m wind speed (u_{10}), surface radiative and turbulent heat fluxes, air temperature, humidity and surface pressure. It enables the calculations of temperature and salinity at the interface (S_{int} and T_{int}) and below the diffusive microlayers ($S_{subskin}$ and $T_{subskin}$).

If the parameterization of $\Delta T_{int} = T_{int} - T_{subskin}$ and $\Delta T_{subskin} = T_{subskin} - T_{fnd}$ has been extensively validated[71], the parameterization of $\Delta S_{subskin} = S_{subskin} - S_{fnd}$ has only been validated against a limited set of in situ observations in the tropics and mid-latitudes[22,30,72]. Yet, fCO^{a}_{2int} is mainly sensitive to temperature and $fCO^{w}_{2subskin}$ to salinity changes[4,32,62]. Therefore, to evaluate the uncertainty of our estimate on the dilution by rain, an alternative parameterization based on satellite measurements[31] is considered to calculate $\Delta S_{subskin}$. We note ΔS_1 the change in subskin salinity obtained with the physical parameterization, previously described, and ΔS_2 the one obtained with the empirical relation deduced from a large set of observations on the globe of surface salinity from SMOS and SMAP. The latter depends on 10 m wind and rain rate from IMERG as follows $\Delta S_2 = b_1 R u_{10}^{-b_2}$, with the coefficients $b_1 = -0.35$ pss (mm h^{-1})$^{-1}$ and $b_2 = 0.77$. This latter parameterization of the salinity gradient below the diffusive microlayer usually leads to stronger rain-induced dilution than the former physically based parameterization[30] (Extended Data Fig. 3c).

Given a rain-induced freshening below the microlayer, changes in $DIC_{subskin}$ and $TAlk_{subskin}$ are then directly calculated from the corresponding changes in $S_{subskin}$[21] as follows:

$$DIC_{subskin} = DIC_{fnd}\left(\frac{S_{subskin}}{S_{fnd}}\right) + DIC_r\left(1 - \frac{S_{subskin}}{S_{fnd}}\right) \quad (5)$$

$$TAlk_{subskin} = TAlk_{fnd}\left(\frac{S_{subskin}}{S_{fnd}}\right) \quad (6)$$

DIC_r is determined using the temperature–solubility relationship[48] and assuming the raindrops are in solubility equilibrium with fCO^{a}_{2} at the wet-bulb temperature, which is a valid substitute for the rain drop temperature at the ocean surface[73]. Thus, $DIC_r = K_0 fCO^{a}_{2}$ with K_0 the aqueous solubility of CO_2 and fCO^{a}_{2} the partial pressure of CO_2 in the atmosphere. Both quantities are calculated for freshwater (that is, $S = 0$) and using the wet-bulb temperature, which can be defined as a function of air temperature and relative humidity[74]. For instance, during SPURS-2, the DIC concentration in raindrops was around $DIC_r = 14.6$ mol kg^{-1} (ref. 21). This correction on the DIC dilution has however only a negligible impact on the calculated rain effects on the global CO_2 sink, reducing around 0.008% the uncorrected flux estimates taking into account rain-induced dilution from 2008 to 2018.

(3) Wet deposition. Finally, following the same assumption of equilibrium between the raindrops and fCO^{a}_{2} in the atmosphere, the wet deposition of CO_2 by rain (F_{WD}) is defined as an additional flux to the classical interfacial flux across the ocean interface (F_{ref} described by equation (3)) and is parameterized as follows[26]:

$$F_{WD} = RK_0 fCO^{a}_{2} \quad (7)$$

with K_0 and fCO^{a}_{2} similarly calculated using the wet-bulb temperature and a salinity set to zero. Contrary to the limitation of the near surface DIC dilution discussed above, this direct deposition of moles of CO_2 in the ocean is a major effect of rain on the CO_2 global sink.

The CO_2 flux diagnostics

The total CO_2 fluxes are defined as follows:

- The reference flux F_{ref} is computed following equations (2) and (3) with the temperature and salinity fields at the interface and below the skin layer calculated using the prognostic model[30] to represent diurnal warm layers and cool skin phenomena but without considering the impact of rain and, thus, with undiluted DIC and TAlk (that is, $DIC_{subskin} = DIC_{fnd}$ and $TAlk_{subskin} = TAlk_{fnd}$).
- The CO_2 flux taking into account the impact of rain-induced turbulence alone is evaluated as F_{ref}, but using equation (4) instead of equation (2) to compute the transfer velocity definition $k_t(600)$. This flux is noted F_{kr}.
- The CO_2 flux taking into account only the rain-induced dilution is diagnosed following equations (2) and (3) with the rain impact on ΔT_{int}, $\Delta T_{subskin}$ and $\Delta S_{int} = S_{int} - S_{subskin}$ diagnosed with the prognostic model[30]. The effect of rain on subskin salinity change $\Delta S_{subskin}$ is diagnosed either as (1) ΔS_1 using the parameterization based on the prognostic model[30] or as (2) ΔS_2 using the satellite-derived parameterization[31] of near-surface dilution. The corresponding fluxes are noted, respectively, as $F^{\Delta S_1}_{DIL}$ and $F^{\Delta S_2}_{DIL}$. The dilution of the DIC and TAlk fields are computed from equations (5) and (6) using the corresponding change in near-surface salinity.
- The interfacial flux, noted $F^{\Delta S_1}_{INT}$ and $F^{\Delta S_2}_{INT}$ depending on the dilution model, takes into account the effects of rain-induced turbulence using equation (4) as F_{kr} and dilution using equation (3) as $F^{\Delta S_1}_{DIL}$ and $F^{\Delta S_2}_{DIL}$.
- The wet deposition F_{WD} is computed following equation (7).
- Total flux ($F^{\Delta S_1}_{TOT}$ and $F^{\Delta S_2}_{TOT}$) is obtained by adding wet deposition F_{WD} to the corresponding interfacial flux $F^{\Delta S_1}_{INT}$ and $F^{\Delta S_2}_{INT}$.

The corresponding rain effects are deduced from the difference between any of these flux diagnostics and F_{ref} and are noted ΔF_{kr}, $\Delta F^{\Delta S_1}_{DIL}$, $\Delta F^{\Delta S_2}_{DIL}$, $\Delta F^{\Delta S_1}_{INT}$, $\Delta F^{\Delta S_2}_{INT}$, $\Delta F^{\Delta S_1}_{TOT}$ and $\Delta F^{\Delta S_2}_{TOT}$, respectively.

All the CO_2 fluxes are computed from 1 January 2008 to 31 December 2018.

We use the foundation sea surface temperature (T_{fnd}), rain rate, surface heat flux, air temperature, humidity, surface pressure and wind speed (u_{10}) from the fifth generation of the European Centre for Medium-Range Weather Forecasts (ECMWF) atmospheric reanalysis of the global climate (ERA5)[36]. These fields are provided at 0.25° horizontal spatial resolution and hourly temporal resolution, except the T_{fnd}, which is daily. The grid cells with a non-zero ice cover from ERA5 as well as the land cells are ignored. The foundation sea surface salinity (S_{fnd}) fields used in the analysis were derived from an interpolation of in situ sea surface salinity data using a multi-dimensional optimal interpolation algorithm[37,38] (multi-observation global ocean sea surface salinity and sea surface density). The product with weekly temporal resolution was chosen and interpolated over the ERA5 grid (0.25°). We also used NOAA Greenhouse Gas Marine Boundary Layer Reference39 for the implementation of the temporal and spatial evolution of the atmospheric CO_2 dry air mole fraction (x_{CO_2}). This product is derived from atmospheric measurements from the NOAA Global Monitoring Laboratory sampling network and originally provides zonally averaged (over 4.5° bands) and weekly estimates, which were linearly interpolated over a 0.25° grid and resampled from weekly to monthly for this study. We use the OceanSODA-ETHZ dataset[40] for the bulk sea surface DIC_{fnd} and $TAlk_{fnd}$ fields, which provide monthly values over the period 1985–2018. The sea surface phosphate and silicate fields are taken from a global monthly climatology of TAlk[75] obtained using a neural network

approach with climatological fields of salinity, temperature and oxygen from the World Ocean Atlas dataset[76]. While originally being on a 1° grid, both of these products were linearly interpolated over a 0.25° grid for this study.

An additional global rain product is considered in this study: the satellite-based rain data from the NASA Global Precipitation Measurement (GPM) product IMERG[41]. It combines rain estimates from multiple passive microwave and infra-red sensors, which are then corrected through gauge rain analyses. The resulting product originally provides estimates of rain rates with a spatial resolution of 0.1° and temporal resolution of 30 min over the whole globe. Here, it has been interpolated over the ERA5 grid (0.25° × 0.25°, 1 h). IMERG has a limited coverage at higher latitudes so computations are restricted to the domain 60° S–60° N.

Data availability

Estimates of the CO_2 fluxes for the different diagnostics done in this study are publicly available at the Zenodo repository at https://doi.org/10.5281/zenodo.12699295 (ref. 77). Reanalysis data from the ECMWF ERA5 model was obtained through the Copernicus Climate Change Service (2023) (https://cds.climate.copernicus.eu/cdsapp#!/dataset/reanalysis-era5-single-levels?tab=overview). The CO_2 dry air mole fraction data were from the NOAA Greenhouse Gas Marine Boundary Layer Reference (https://gml.noaa.gov/ccgg/mbl/data.php). The foundation salinity values have been downloaded from EU Copernicus Marine Service Information (https://doi.org/10.48670/moi-00051). Global DIC and TAlk bulk values was obtained from the OceanSODA–ETHZ climatology dataset (https://www.ncei.noaa.gov/access/metadata/landing-page/bin/iso?id=gov.noaa.nodc:0220059). The IMERG satellite-derived precipitation data were provided by the NASA/Goddard Space Flight Center's and PPS, which develop and compute the IMERG as a contribution to GPM, and archived at the NASA GES DISC (https://doi.org/10.5067/GPM/IMERG/3B-HH/07).

Code availability

The prognostic ocean skin model (Bellenger et al.[30]) is open-access and can be downloaded at https://gitlab.in2p3.fr/ipsl/lmd/dpao/ocean-skin.

References

42. Wanninkhof, R. Relationship between wind speed and gas exchange over the ocean revisited. *Limnol. Oceanogr. Methods* **12**, 351–362 (2014).
43. Jähne, B., Heinz, G. & Dietrich, W. Measurement of the diffusion coefficients of sparingly soluble gases in water. *J. Geophys. Res. Oceans* **92**, 10767–10776 (1987).
44. Wanninkhof, R. Relationship between wind speed and gas exchange over the ocean. *J. Geophys. Res. Oceans* **97**, 7373–7382 (1992).
45. Wanninkhof, R. & McGillis, W. R. A cubic relationship between air–sea CO_2 exchange and wind speed. *Geophys. Res. Lett.* **26**, 1889–1892 (1999).
46. Nightingale, P. D. et al. In situ evaluation of air–sea gas exchange parameterizations using novel conservative and volatile tracers. *Glob. Biogeochem. Cycles* **14**, 373–387 (2000).
47. Ho, D. T. et al. Measurements of air-sea gas exchange at high wind speeds in the Southern Ocean: implications for global parameterizations. *Geophys. Res. Lett.* **33**, 2006GL026817 (2006).
48. Weiss, R. F. Carbon dioxide in water and seawater: the solubility of a non-ideal gas. *Mar. Chem.* **2**, 203–215 (1974).
49. Weiss, R. F. & Price, B. A. Nitrous oxide solubility in water and seawater. *Mar. Chem.* **8**, 347–359 (1980).
50. Orr, J. C. & Epitalon, J.-M. Improved routines to model the ocean carbonate system: mocsy 2.0. *Geosci. Model Dev.* **8**, 485–499 (2015).
51. Waters, J. F. & Millero, F. J. The free proton concentration scale for seawater pH. *Mar. Chem.* **149**, 8–22 (2013).
52. Uppström, L. R. The boron/chlorinity ratio of deep-sea water from the Pacific Ocean. *Deep Sea Res* **21**, 161–162 (1974).
53. Dickson, A. G., Sabine, C. L. & Christian, J. R. *Guide to Best Practices for Ocean CO_2 Measurements*. (North Pacific Marine Science Organization, 2007).
54. Stommel, H. Observations of the diurnal thermocline. *Deep Sea Res* **16**, 269–284 (1969).
55. Soloviev, A. & Lukas, R. *The Near-Surface Layer of the Ocean: Structure, Dynamics and Applications* (eds Mysak, L. A.) (Springer, 2014).
56. Fairall, C. W. et al. Cool-skin and warm-layer effects on sea surface temperature. *J. Geophys. Res. Oceans* **101**, 1295–1308 (1996).
57. Stuart-Menteth, A. C., Robinson, I. S. & Challenor, P. G. A global study of diurnal warming using satellite-derived sea surface temperature. *J. Geophys. Res. Oceans* **108**, 2002JC001534 (2003).
58. Bellenger, H. & Duvel, J.-P. An analysis of tropical ocean diurnal warm layers. *J. Clim.* **22**, 3629–3646 (2009).
59. Saunders, P. M. The temperature at the ocean–air interface. *J. Atmos. Sci.* **24**, 269–273 (1967).
60. Yu, L. On sea surface salinity skin effect induced by evaporation and implications for remote sensing of ocean salinity. *J. Phys. Oceanogr.* **40**, 85–102 (2010).
61. Bolin, B. On the exchange of carbon dioxide between the atmosphere and the sea. *Tellus* **12**, 274–281 (1960).
62. McGillis, W. R. & Wanninkhof, R. Aqueous CO_2 gradients for air–sea flux estimates. *Mar. Chem.* **98**, 100–108 (2006).
63. Robertson, J. E. & Watson, A. J. Thermal skin effect of the surface ocean and its implications for CO_2 uptake. *Nature* **358**, 738–740 (1992).
64. Dong, Y. et al. Update on the temperature corrections of global air–sea CO_2 flux estimates. *Glob. Biogeochem. Cycles* **36**, e2022GB007360 (2022).
65. Fay, A. R. et al. SeaFlux: harmonization of air–sea CO_2 fluxes from surface pCO_2 data products using a standardized approach. *Earth Syst. Sci. Data* **13**, 4693–4710 (2021).
66. Harrison, E. L. et al. Nonlinear interaction between rain- and wind-induced air–water gas exchange. *J. Geophys. Res. Oceans* **117**, C03034 (2012).
67. Ho, D. T. et al. The combined effect of rain and wind on air–water gas exchange: a feasibility study. *J. Mar. Syst.* **66**, 150–160 (2007).
68. Zappa, C. J. et al. Rain-induced turbulence and air–sea gas transfer. *J. Geophys. Res. Oceans* **114**, 2008JC005008 (2009).
69. Schlüssel, P., Soloviev, A. V. & Emery, W. J. Cool and freshwater skin of the ocean during rainfall. *Bound. Layer Meteorol.* **82**, 437–472 (1997).
70. Zeng, X. & Beljaars, A. A prognostic scheme of sea surface skin temperature for modeling and data assimilation. *Geophys. Res. Lett.* **32**, L14605 (2005).
71. Luo, B. & Minnett, P. J. Evaluation of the ERA5 sea surface skin temperature with remotely-sensed shipborne marine–atmospheric emitted radiance interferometer data. *Remote Sens* **12**, 1873 (2020).
72. Witte, C. R., Zappa, C. J. & Edson, J. B. The response of ocean skin temperature to rain: observations and implications for parameterization of rain-induced fluxes. *J. Geophys. Res. Oceans* **128**, e2022JC019146 (2023).
73. Gosnell, R., Fairall, C. W. & Webster, P. J. The sensible heat of rainfall in the tropical ocean. *J. Geophys. Res. Oceans* **100**, 18437–18442 (1995).
74. Stull, R. Wet-bulb temperature from relative humidity and air temperature. *J. Appl. Meteorol. Climatol.* **50**, 2267–2269 (2011).

75. Broullón, D. et al. A global monthly climatology of total alkalinity: a neural network approach. *Earth Syst. Sci. Data* **11**, 1109–1127 (2019).
76. Boyer, T. P. et al. *World Ocean Database 2013* (US Department of Commerce, National Oceanic and Atmospheric Administration, National Environmental Satellite, Data, and Information Service, National Oceanographic Data Center, Ocean Climate Laboratory, 2013).
77. Parc, L. et al. Global ocean carbon uptake enhanced by rainfall : CO_2 flux datasets. *Zenodo* https://doi.org/10.5281/zenodo.12699295 (2024).

Acknowledgements

This study benefited from the Institut Pierre-Simon Laplace Data and Computing Center Ensemble de Services Pour la Recherche à l'IPSL, which is supported by the Centre National de la Recherche Scientifique, Sorbonne Université, Centre National d'Etudes Spatiales and Ecole Polytechnique. This work was supported by the Chanel Research Chair: Understanding the Linkages between the Ocean, the Carbon Cycle, and Marine Ecosystems under Climate Change, which partly funded the PhD of L.P. L.B. acknowledges funding from the European Union's Horizon 2020 research and innovation programme under grant agreement no. 101003536 (project ESM2025). The results contain modified Copernicus Climate Change Service information 2020. Neither the European Commission nor ECMWF is responsible for any use that may be made of the Copernicus information or data it contains.

Author contributions

D.T.H., H.B., L.B. and L.P. initiated the design of the study that led to this paper. L.P. and X.P. conducted the calculations. With advice from H.B., L.P. led the analysis and designed the figures. L.P. wrote the article with input from H.B., L.B. and D.T.H. All authors discussed and contributed intellectually to interpretation of the results.

Competing interests

The authors declare no competing interests.

Additional information

Extended data is available for this paper at https://doi.org/10.1038/s41561-024-01517-y.

Correspondence and requests for materials should be addressed to Laetitia Parc or Hugo Bellenger.

Peer review information *Nature Geoscience* thanks Chris Fairall and John Prytherch for their contribution to the peer review of this work. Primary Handling Editor: James Super, in collaboration with the *Nature Geoscience* team.

https://doi.org/10.1038/s41561-024-01517-y

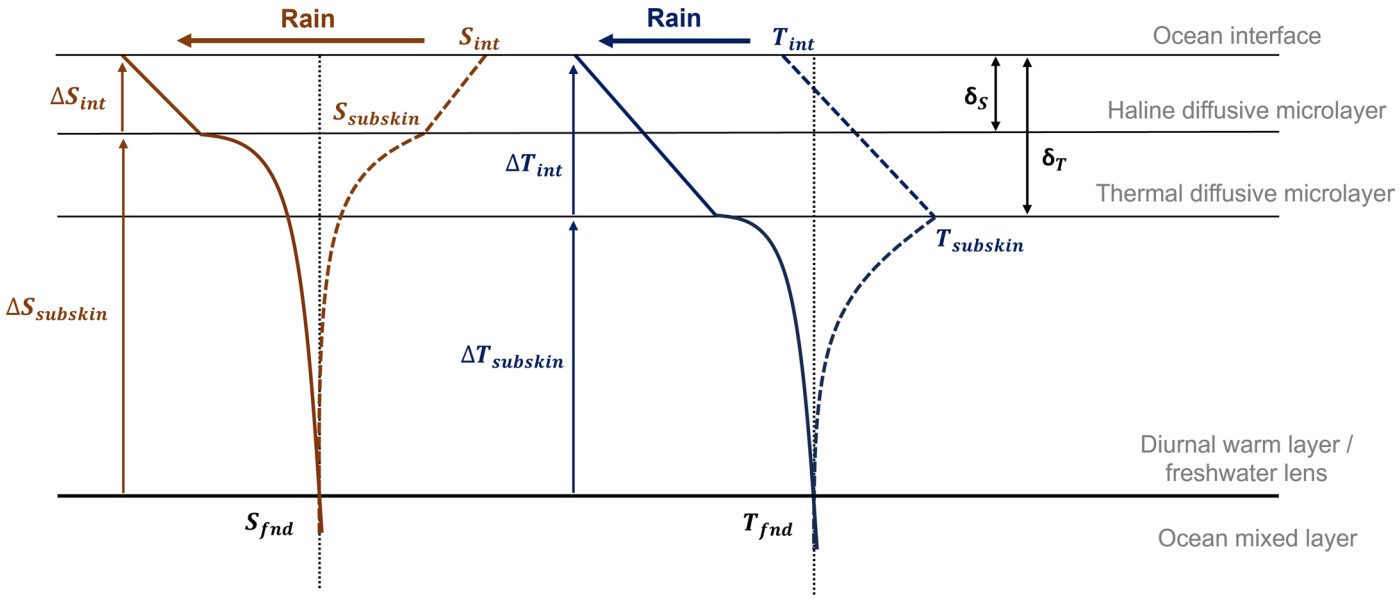

Extended Data Fig. 1 | The thermohaline stratification at the air-sea interface. Temperature (blue) and salinity (orange) profiles for a usual daylight situation (dashed lines) and in the case of the formation of rain-induced freshwater lenses (full lines). Across the diffusive microlayers, the temperature gradient $\Delta T_{\mathrm{int}} = T_{\mathrm{int}} - T_{subskin}$ and salinity gradient $\Delta S_{\mathrm{int}} = S_{\mathrm{int}} - S_{subskin}$ are defined, while $\Delta T_{subskin} = T_{subskin} - T_{fnd}$ and $\Delta S_{subskin} = S_{subskin} - S_{fnd}$ represent the temperature and salinity variations in the near-surface, respectively.

https://doi.org/10.1038/s41561-024-01517-y

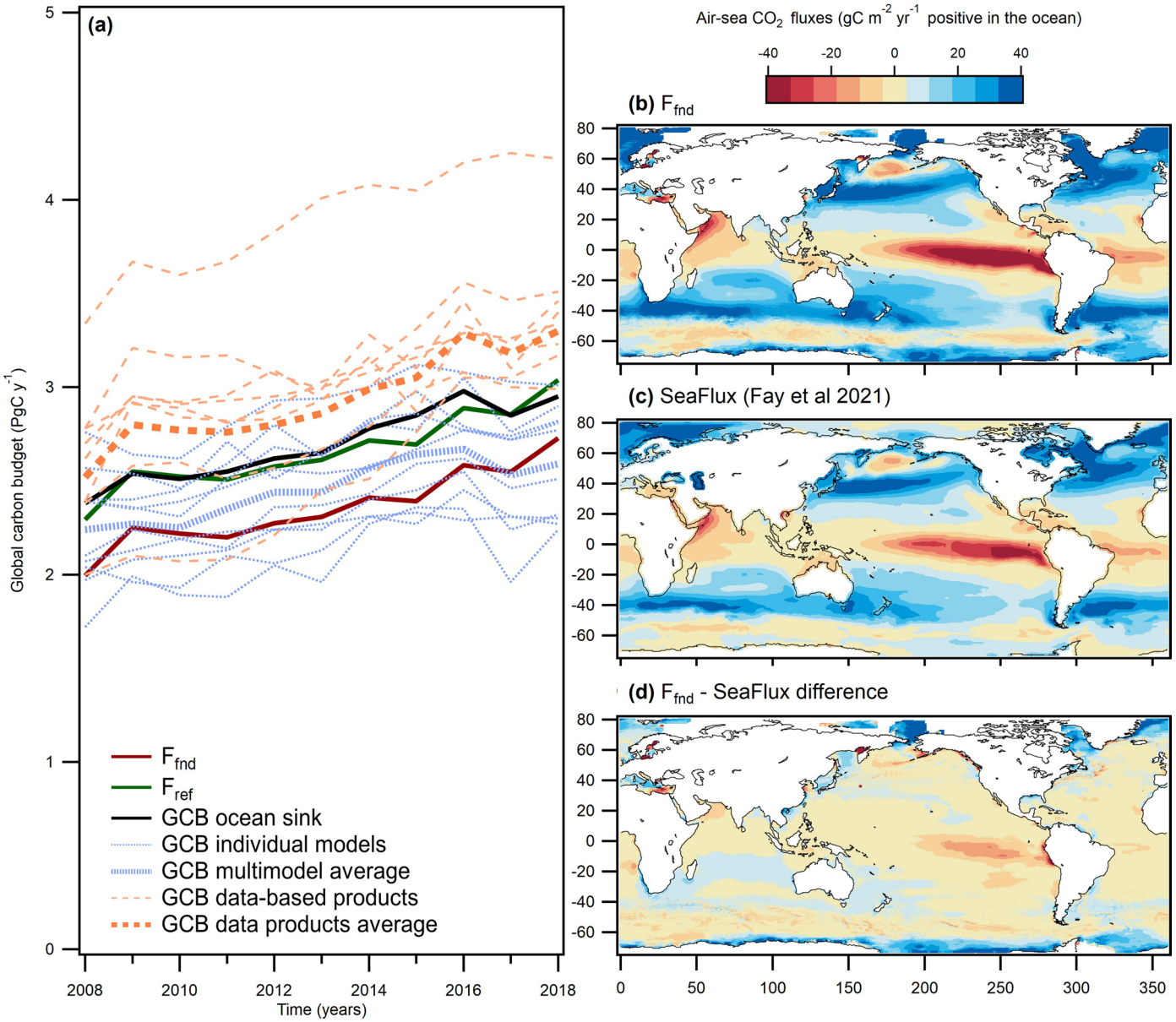

Extended Data Fig. 2 | The global ocean carbon sink. (a) Time series of the global annual mean CO_2 sink (PgC yr^{-1}) from the Global Carbon Budget[1] based on data products (dashed orange lines), individual models (dashed blue lines) and on models and data products (full black line) and calculated from F_{fnd} (full red line) and from F_{ref} (full green line). Maps of mean air-sea CO_2 fluxes between 2008 and 2018 (positive into the ocean, colors) from **(b)** F_{fnd} and **(c)** the SeaFlux data product average[65] for the 6 interpolation methods for the pCO_2 maps and 5 wind products and **(d)** the difference between F_{fnd} and the SeaFlux product. Only the air-sea carbon flux differences that are statistically significant at the 99% level estimated by the Student's *t*-test are plotted.

https://doi.org/10.1038/s41561-024-01517-y

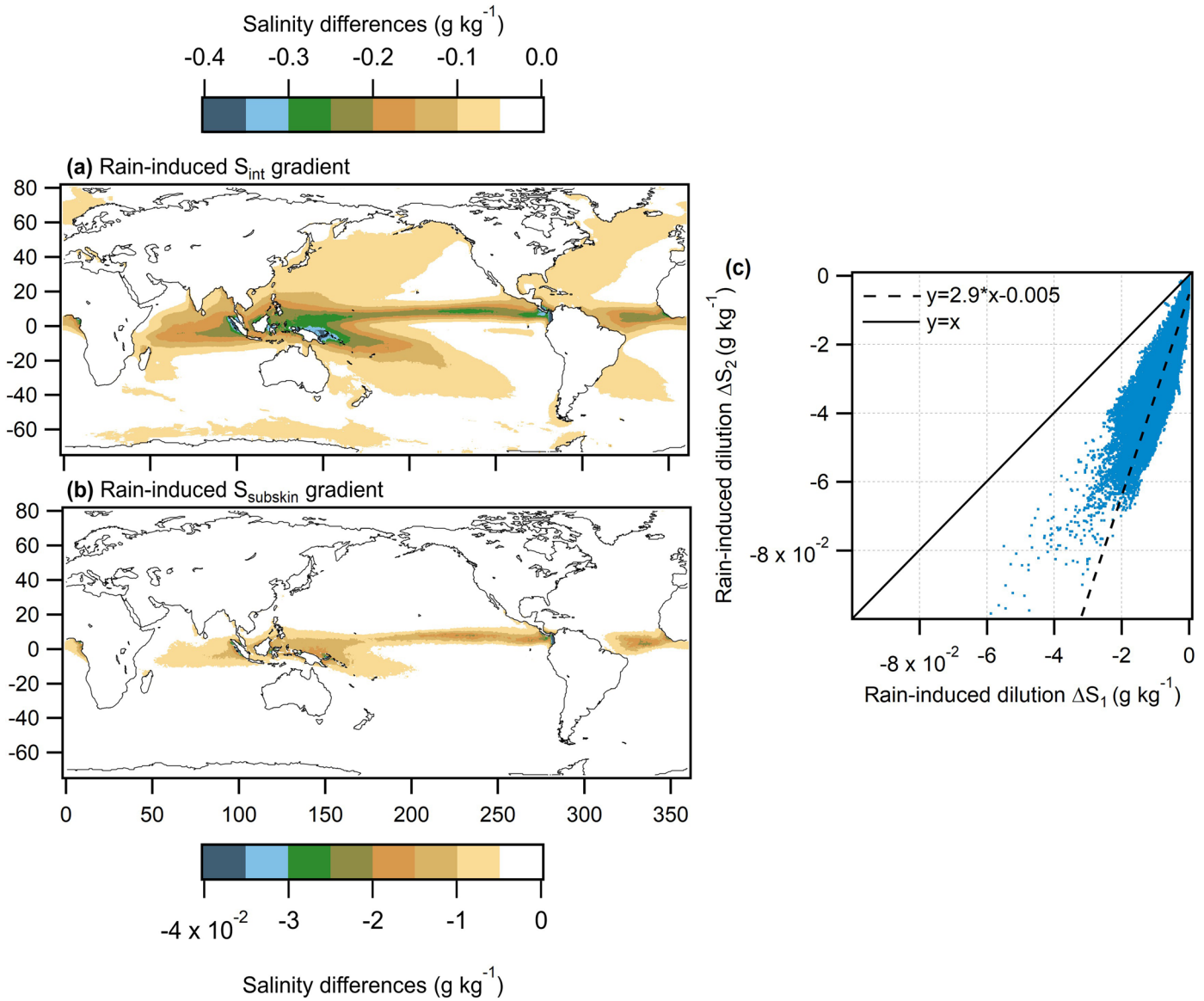

Extended Data Fig. 3 | The rain-induced salinity changes. Maps of mean rain-induced differences in salinity (g kg^{-1}) **(a)** at the ocean interface and **(b)** at the base of the haline diffusive microlayer calculated using the prognostic scheme[30] ΔS_1 over the 11-year period. **(c)** Scatterplot of the 2008-2018 mean salinity differences due to rain below the diffusive microlayer ($\Delta S_{subskin}$, g kg^{-1}) from the satellite-derived empirical relationship[31] (ΔS_2) and from the physically-based parametrization[30] (ΔS_1).

https://doi.org/10.1038/s41561-024-01517-y

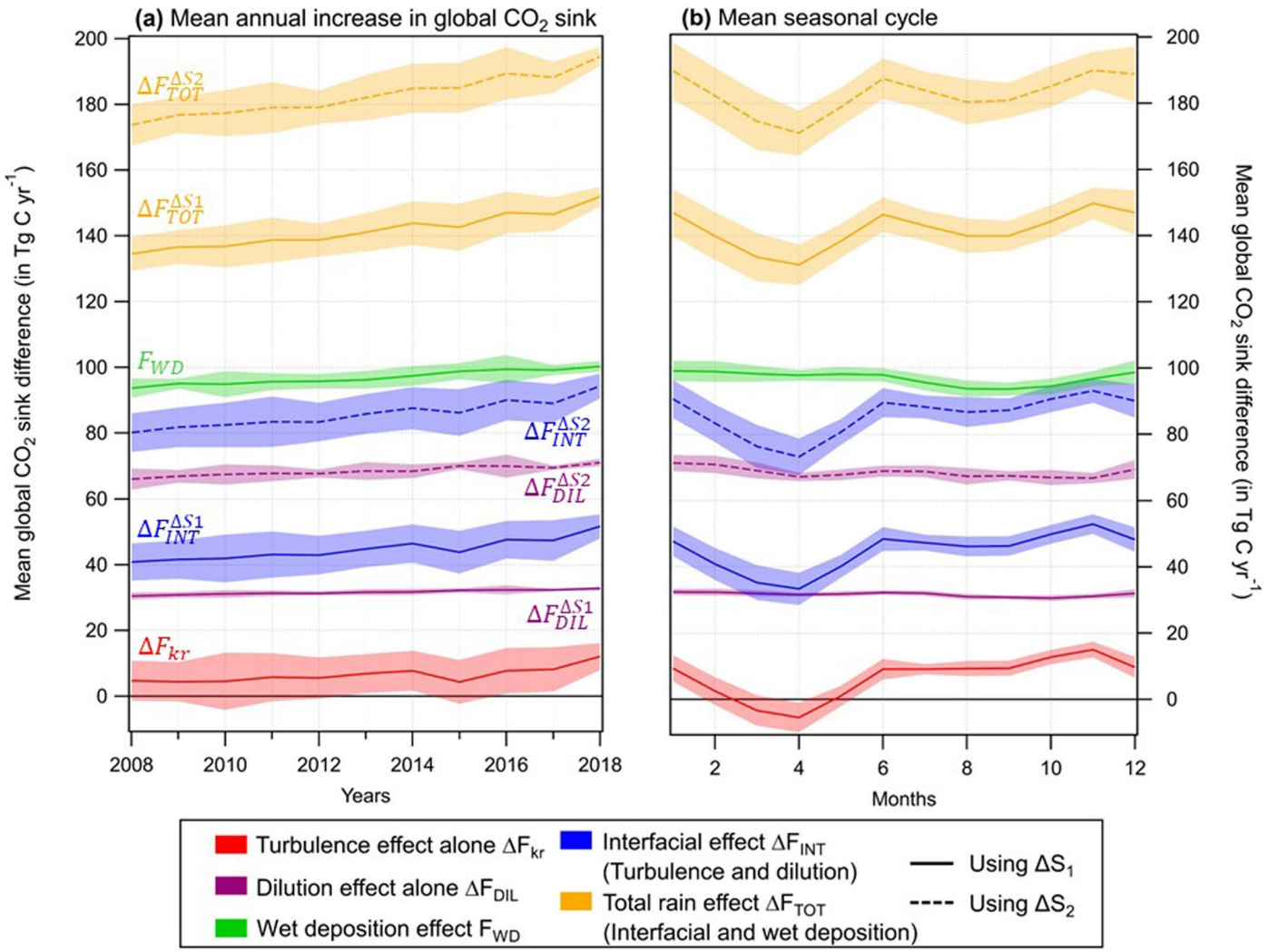

Extended Data Fig. 4 | Sensitivity of the rain effects to the dilution model. **(a)** Time series of the annual mean global ocean CO_2 sink differences (TgC yr^{-1}, left axis) due to the rain-induced turbulence effect ΔF_{kr} (red), the wet deposition effect F_{WD} (green), the rain-induced dilution effect ΔF_{DIL} (purple), the interfacial rain effect ΔF_{INT} (blue) and to the total rain effect ΔF_{TOT} (orange), with the rain-induced dilution in these three latter contributions being either based on a prognostic scheme[30] ΔS_1 (full lines) or the satellite-derived empirical parametrization[31] ΔS_2 (dashed lines) (shadings are the intra-annual standard deviation of the corresponding differences). **(b)** Time series of the monthly mean seasonal cycle of global CO_2 sink differences (TgC yr^{-1}, colors are as in (a), shading represents the inter-annual standard deviation for each month).

https://doi.org/10.1038/s41561-024-01517-y

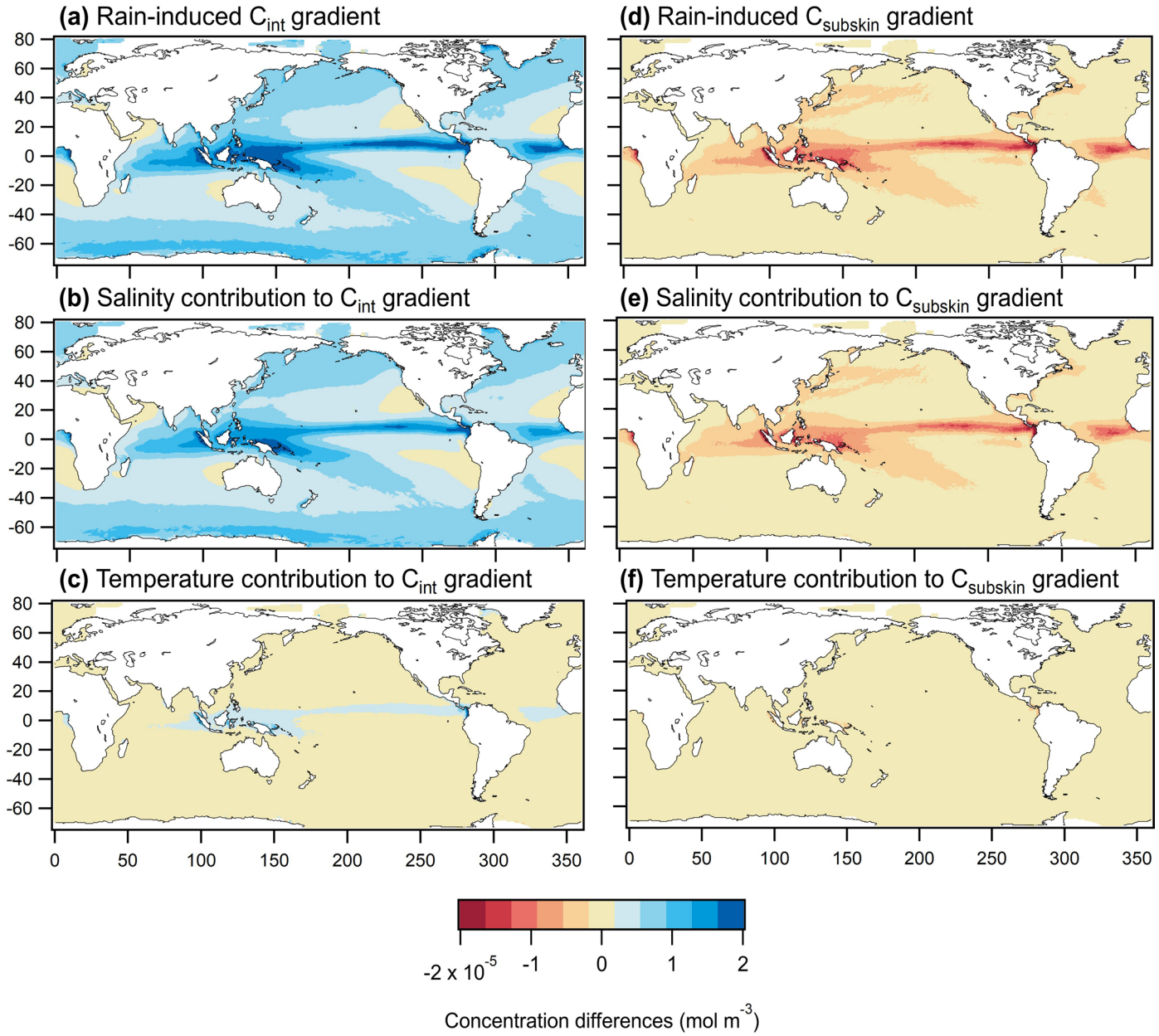

Extended Data Fig. 5 | Spatial distribution of rain-induced CO_2 concentration changes. Mean maps of rain-induced CO_2 concentration differences (mol m^{-3}) at **(a)** the interface and **(d)** the bottom of the diffusive microlayer using a prognostic scheme[30] ΔS_1 for the parametrization of the corresponding temperature and salinity gradients over the period 2008-2018. Mean maps of the salinity ((**b**) and (**e**)) and temperature ((**c**) and (**f**)) contributions to the rain-induced CO_2 concentration differences (mol m^{-3}) at the interface ((**b**) and (**c**)) and at the bottom of the diffusive microlayer ((**e**) and (**f**)) over the period 2008-2018. Approximate formulations are used for the changes in CO_2 concentrations at the interface and below the haline diffusive microlayer (C_{int} and $C_{subskin}$ respectively) due to rain-induced temperature and salinity gradients across the corresponding diffusive microlayer, and between the base of the diffusive microlayers and the top of the mixed layer. It enables an assessment of their respective contributions to the CO_2 concentration gradients. The details on the calculations of the total derivatives of $C_{int} = K_0^a(T,S)fCO_2^a(T,S)$ and $C_{subskin} = K_0^w(T,S)fCO_2^w(T,S,DIC,TAlk)$ can be found in former studies[4,49,62].